Journal of Solid State Chemistry **155,** 394–408 (2000)
doi:10.1006/jssc.2000.8940, available online at http://www.idealibrary.com on IDEAL®

TEM Studies: The Key for Understanding the Origin of the 3.3 V and 4.5 V Steps Observed in $LiMn_2O_4$-based Spinels

L. Dupont,*,[1] M. Hervieu,† G. Rousse,‡ C. Masquelier,‡ M. R. Palacín,§ Y. Chabre,⊥ and J. M. Tarascon*

*Laboratoire de Réactivité et de Chimie des Solides (UPJV), 33 rue Saint Leu, F-80039, Amiens, France; †Laboratoire de Cristallographie et Sciences des Matériaux (CNRS) ISMRA, Bld. du Maréchal Juin, 14050 Caen, France; ‡Laboratoire de Chimie des Solides, Université de Paris-XI Orsay, Bat. 414, 91405 Orsay, Paris 33, France; §Institut de Ciència de Materials de Barcelona (CSIC) Campus UAB, E-08193 Bellaterra, Spain; and ⊥LSP, UJF-Grenoble and CNRS, BP 87, F-38402, St. Martin d'Hères, France

Received April 24, 2000; in revised form August 4, 2000; accepted August 8, 2000; published online November 29, 2000

Transmission electron microscopy (TEM) measurements were performed on electrochemically partially delithiated prepared spinel $Li_{1-x}Mn_2O_4$ samples. The potential–composition profile of $LiMn_2O_4$ exhibits (besides the two plateaus at 4.05 and 4.1 V) two additional redox steps of identical capacity at 4.5 and 3.3/3.95 V. We found by TEM studies that these extra steps are the signature of a reversible phase transition between $LiMn_2O_4$ spinel type structure and a new $Li_{1-x}Mn_2O_4$ double hexagonal (DH) type structure ($a \approx 5.8$ Å, $c \approx 8.9$ Å, $P6_3mc$). The latter is isotypic with DH $LiFeSnO_4$. Selected area electron diffraction (SAED) and high-resolution transmission electron microscopy (HRTEM) made it possible to identify the mechanism by which this cubic–DH phase transition occurs within a particle. Based on the structural findings the origin as well as the similar electrochemical capacity of the 3.3/3.95 and 4.5 V anomalies are explained.

Key Words: **$LiMn_2O_4$; 3.3 V plateau, electrochemistry; TEM.**

INTRODUCTION

In recent years, a strong dependence between the $LiMn_2O_4$ synthesis route and its electrochemical properties has been noted. The potential composition profile of the $LiMn_2O_4$ spinel that was proposed to be used as an alternative to $LiCoO_2$ in commercial lithium ion batteries exhibits two large reversible plateaus at 4.05 and 4.1 V upon lithium extraction/reinsertion. However, two additional redox steps of identical capacity at 4.5 and 3.3/3.95 V could be observed (1–3) depending upon the synthesis conditions and thermal history of the samples. These extra plateaus are detrimental to the cycling capacity retention of $LiMn_2O_4$ samples. Given the practical implications of this subject, numerous authors tried to understand the origin of the phenomenon (1–5). The results emerging from these studies can be summarized as follows. First, regardless of whether the starting materials were showing the 3.3/4.5 V anomalies, they could not be differentiated by usual solid-state characterization techniques such as X-ray diffraction, atomic absorption, and electron diffraction. Second, it was noted that both extra redox steps always appeared together with the same capacity. Various unsatisfactory hypotheses were proposed to explain these unusual 3.3 and 4.5 V phenomena. Among them were the mixing of Li and Mn cations on spinel 8*a* sites (4) and the existence of oxygen vacancies (1, 3) proposed by Tarascon *et al.* and Dahn *et al.*, respectively.

Finally, it was recently shown, through *in situ* synchroton X-ray diffraction studies, that these extra redox steps were linked to the appearance/disappearance of extra reflections. Because of their limited number and weak intensities, attempts to index them turned out to be unsuccessful (6, 7). Therefore, from the peaks' splitting and broadening the occurrence of a cubic cell distortion was deduced together with a decrease in the material's crystallinity (7).

To clarify this issue, we searched whether structural defects, stacking faults, twinning, or others could be at the origin of these electrochemical anomalies. From previous studies on differently made $LiMn_2O_4$ samples (6, 8) we were able to draw a correlation between the sample's physical and electrochemical behavior. For instance, samples exhibiting at low temperature a Jahn–Teller transition will present the 3.3 V/4.5 V steps and vice versa. This transition was recently monitored by cooling the sample in a transmission electron microscope (TEM) and an orthorhombic (9) rather than a tetragonal phase as previously believed (10, 11) was unambiguously evidenced. On the basis of that success, we decided to perform transmission electron microscopy studies on samples that were electrochemically prepared in various redox states in order to understand the origin of the 3.3 and 4.5 V anomalies.

[1]To whom correspondence should be addressed. E-mail: loic.dupont@sc.u-picardie.fr.

0022-4596/00 $35.00

A first part of this study that was already published (8) led to the conclusion that the origin of the 3.3 and 4.5 V peaks was nested in the existence of a cubic–double hexagonal phase transition. Herein, we further look at the structural details of this transition that was previously observed in other systems such as $LiFeSnO_4$ (12, 13).

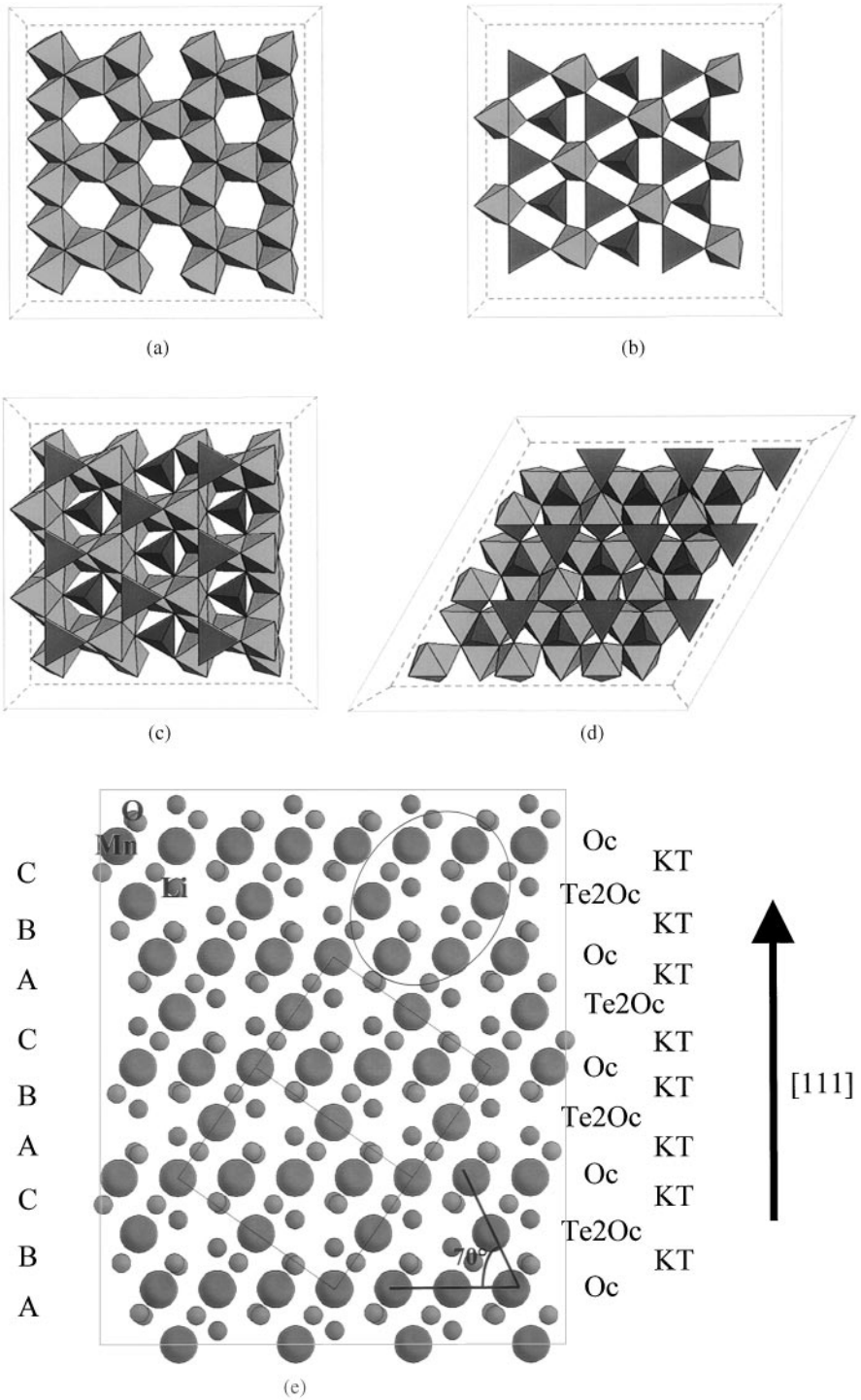

FIG. 1. Structural units forming the spinel and double hexagonal structures: (a) Oc_3, kagome MnO_6 octahedral layer; (b) Te_2Oc, MnO_6 octahedra and LiO_4 tetrahedra mixed layer; (c) $J_{K/T}$ junction obtained by blocking a kagome window with a tetrahedron; (d) $J_{K/O}$ junction obtained by blocking a kagome window with an octahedron. (e, f) Structural drawing of spinel and double hexagonal structures respectively showing the relationships between oxygen close-packing (ABC and ABAC respectively), layers (Oc_3 and Te_2Oc), and junctions (KT and KO). Manganese, oxygen, and lithium atoms are shown as large, medium, and small spheres, respectively. Note the 70° between two equivalent (111) planes for the spinel structure.

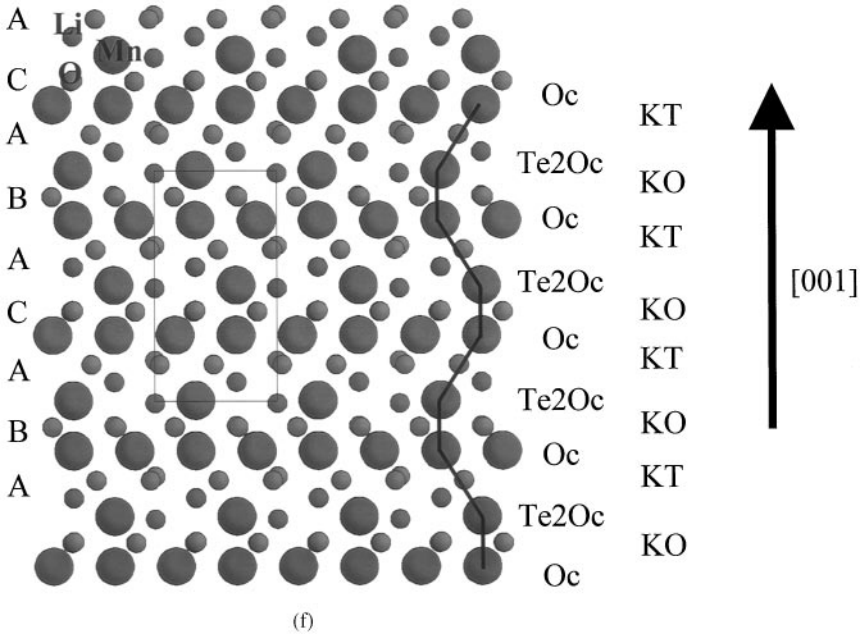

FIG. 1—*Continued*

EXPERIMENTAL METHODS

Synthesis

Stoichiometric $LiMn_2O_4$ was prepared in air at 800–850°C from Li_2CO_3 and β-MnO_2 as reported in Ref. 9 or 15. The resulting $LiMn_2O_4$ sample was found to be cubic and single phase $a = 8.2495(2)$ Å at 350 K. This sample presents the charge ordering around 20°C as determined by electron diffraction or differential scanning calorimetry (DSC) upon cooling (9). The TEM observations were consistent with the X-ray diffraction results.

Electrochemistry

Electrochemical experiments were performed using Swagelok type cells (16). The positive electrode was usually prepared by mixing the $LiMn_2O_4$ powder with 10% (weight) black carbon (SP from MMM, Belgium). A 1 M $LiPF_6$ ethylene carbonate (EC)–dimethyl carbonate (DMC) solution was used as the electrolyte and a lithium foil as the negative electrode. The $LiMn_2O_4$/electrolyte/Li cells were tested on a MacPile multichannel potentiostat/galvanostat (Bio-Logic Co., Claix, France). Room temperature galvanostatic cycling was usually performed between 2.8 and 4.8 V at a rate of $C/50$. After cycling, the cells were disassembled in a glove box, and the $Li_xMn_2O_4$ $(0.1 < x < 1)$ sample powders were recovered, washed with pure DMC to remove electrolyte traces, and investigated by both TEM and powder X-ray diffraction.

Transmission Electron Microscopy

A small amount of the washed powder was dispersed by manual grinding in 1-butanol. A drop of the suspension was collected on a holey carbon film supported on a Cu grid. The selected area electron diffraction (SAED) study was performed with a JEOL 200CX electron microscope fitted with a eucentric goniometer ($\pm 60°$). The high-resolution transmission electron microscopy (HRTEM) study was performed with a TOPCON 002B microscope having a point resolution of 1.8 Å.

Powder Diffraction Techniques

X-ray diffraction was performed on Philips PW1710 diffractometer with Cu $K\alpha$ monochromatic radiation. The X-ray diffraction pattern was checked for each of the samples studied by TEM. Phases' cell parameters were refined using Fullprof software (17). Lazy-pulverix software (18) was used to index the reflections of the complex biphasic X-ray patterns.

RESULTS AND DISCUSSION

(1) Structure Description

For the sake of understanding, it is useful to start from an appropriate description of the spinel structure (denoted S) and of its derived structures in terms of oxygen close-packing and layer stacking (12).

In terms of oxygen atoms close-packing, the stacking sequence for the spinel along $[111]_{(S)}$ is (ABCABC), and the

sites' occupancy factors are 1/2 for octahedral sites and 1/8 for tetrahedral sites. The structure, however, can also be described as the stacking of two different types of polyhedral layers: a cation-deficient MnO_6 octahedral layer denoted kagome (14) noted Oc_3 (Fig. 1a), and a mixed MnO_6 octahedra/LiO_4 tetrahedra layer denoted Te_2Oc (Fig. 1b). By this description the (ABC) oxygen layer stacking encountered in the spinel is obtained by blocking a kagome window of Oc_3 layer with a tetrahedron of Te_2Oc layer (Fig. 1c), and is denoted $J_{K/T}$.

Following this description, the blocking of a kagome window of the Oc_3 layer with an octahedron of Te_2Oc layer could be imagined (Fig. 1d) leading to the so-called $J_{K/O}$ junction that corresponds to (ABA) oxygen layer stacking. The outcome of the stacking of these different layers is the creation of two other "hypothetical" structures. The first is characterized by the alternation of $J_{K/T}$ and $J_{K/O}$ junctions leading to an (ABAC) oxygen stacking. This structure, called double hexagonal (DH), was reported in the lithium stannoferrites. The other structure, made only of K/O junctions, results in the (ABAB) oxygen stacking typical of a hexagonal close-packing. Such a structure, to our knowledge, has not been synthesized in AB_2O_4 systems yet.

For clarity, the relationships between oxygen close-packing, layers, junctions, double layer, cubic (c), or hexagonal (h) sequences are highlighted in Fig. 1e,1f.

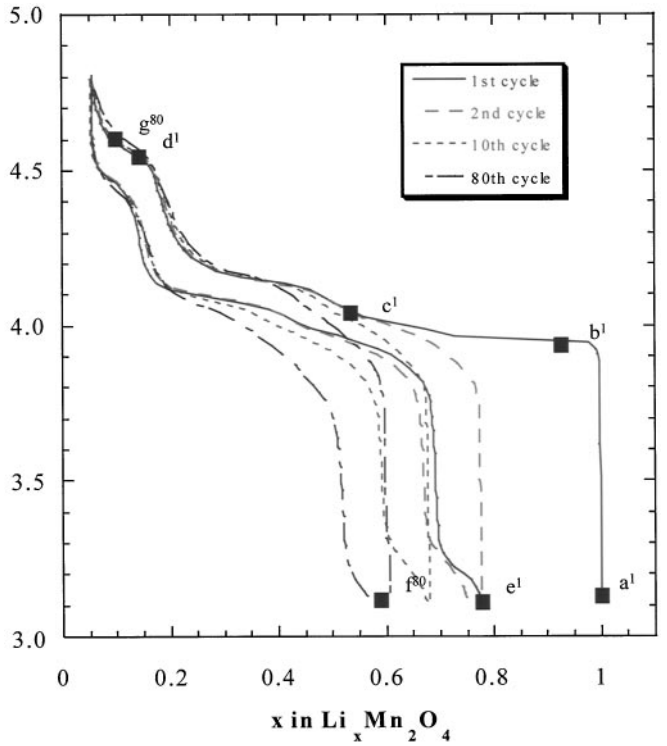

FIG. 2. Voltage composition profile of $LiMn_2O_4$ showing, for each studied sample, the voltage cut after which the different electrochemical cells were opened in order to gather the corresponding powders. Each sample is labeled by a letter in alphabetical order and by an exponent referring to the cycle number.

(2) Ex-Situ Diffraction Experiments

Several $Li_xMn_2O_4$/Li batteries were made, charged, and discharged in a galvanostatic mode at $C/50$ rate (1 lithium per formula unit in 50 hours). The batteries were opened at different states of charge (Fig. 2). The powders were then recovered, washed, and X-rayed (Fig. 3). Additional peaks appeared and grew upon oxidation (Figs. 3b–3d) while they vanished when the reduction of the 3.3 V step was completed (Fig. 3e). Meanwhile, spinel reflections (Fig. 3a) were displaced toward high angles (Figs. 3b–3d) during oxidation and back toward small angles during reduction in agreement with previous studies. It is worth noting that this reversibility on X-ray patterns is still observed after 80 cycles (Figs. 3f, 3g). Nevertheless, it is only when the results of the TEM investigations are used, as explained below, that the extra set of lines was assigned to different structural features. For these samples, the average compositions deduced from electrochemistry, together with the main X-ray diffraction observations and TEM investigation highlights, are listed in Table 1.

(3) Characterization of the Starting Material $LiMn_2O_4$

The starting $LiMn_2O_4$, made similarly to the sample used to observe the cubic–orthorhombic phase transition around room temperature in stoichiometric spinel (9), was first characterized. Rietveld refinements of neutron diffraction on the starting stoichiometric sample (9) confirmed the cubic symmetry ($Fd\bar{3}m$, $a = 8.2495(2)$ Å at 350 K) and oxygen stoichiometry of 3.972(26). This last value was corroborated by redox titration and atomic absorption. The X-ray diffraction pattern (Fig. 3a) does not show any sample evolution with the storage time. TEM studies confirmed that initial particles are a structural faults-free spinel phase. According to the description of the DH structure given in previous literature and summarized above, the $[100]_{(S)}$ and $[111]_{(S)}$ zone axes as well as SAED patterns holding the $[111]^*_{(S)}$ direction were selected to monitor their evolution during the electrochemically induced structural transformation processes. In order to shed light on the evolution of the ED patterns and to allow comparison, the experimental $[001]_{(S)}$ and $[1\bar{1}0]_{(S)}$ SAED patterns, realized on the starting material, are given in Figs. 4a and 4b, respectively.

(4) $Li_{0.9}Mn_2O_4$ Sample

As soon as lithium ions are removed from the spinel host ($Li_{0.9}Mn_2O_4$, b^1 sample), the images evidence the appearance of faults along the $[111]_{(S)}$ direction (Fig. 5a). This is

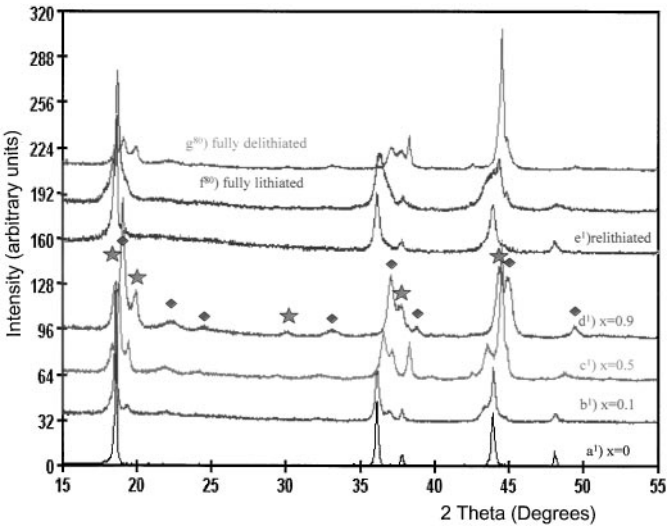

FIG. 3. X-ray diffraction patterns realized on $Li_{1-x}Mn_2O_4$: (a^1) staring material $x = 0$; (b^1) after first oxidation up to $x = 0.1$; (c^1) after first oxidation up to $x = 0.5$; (d^1) after first oxidation up to $x = 0.9$; (e^1) after complete oxidation and then complete reduction; (f^{80}) after the 80th cycle, battery stopped after reduction; (g^{80}) after the 80th cycle, battery stopped after complete oxidation. Lozenges denote the spinel lines that shift with deintercalation. Stars denote new peaks growing upon oxidation and disappearing upon complete reduction.

perfectly consistent with diffuse lines appearing along the $[111]_{(S)}$ direction on the $[1\bar{1}0]_{(S)}$ SAED (Fig. 5b) as well as spots that become starry on the $[100]_{(S)}$ SAED pattern (Fig. 5c), indicating disorder along the direction of a stacking layer and a cubic cell distortion, respectively. The starry spots are most likely due to the presence of several domains in the selected area behaving differently during delithiation: the delithiation of the spinel cells follows the solid solution rule without distortion on some regions while distortion is observed on other twinned regions. This phenomenon is assumed to be associated with the nucleation of a new phase. In addition, the 200 spot (noted by white dashed arrows), with variable intensity, is observed on SAED patterns, confirming the spinel symmetry loss (*d* mirror loss in $Fd\bar{3}\,m$). This nucleation stage is sufficient to induce a first extra reflection on the X-ray diffraction pattern (Fig. 3b) as well as a broadening of the spinel reflections.

From these observations, it appears that the phase nucleation and consequently its growth take place with the spinel cell distortion and, second, that the Te_2Oc layer acts as nucleation planes during the transformation process.

(5) $Li_{0.5}Mn_2O_4$ Sample

Upon further delithiation of the spinel (c^1 sample), as shown on the bright field image realized along $[1\bar{1}0]$ (Figs. 6a, 6b), the new phase growth spreads by sliding of the kagome or Te_2Oc layers. Hence, at this stage, the sample could be described as the intergrowth of new phase domains in a spinel-like distorted matrix. The observed growth periodicity ranges between 81 and 110 Å while the intergrowth domain thickness is mainly equal to 27 Å (pointed by filled black arrows in Fig. 6a) and sometimes equal to 14 Å (dashed arrow in Fig. 6a). These two last distances will be linked to structural features in the HRTEM section. The growth of these domains is responsible for the X-ray powder pattern evolution of the sample, namely the appearance of more extra reflections while others become sharper (Fig. 3c). For the apparently unaffected regions, the spinel cell parameters (as deduced from the X-ray powder pattern) decrease continuously, obeying a solid solution deintercalation mechanism.

The previous samples have so far shown an intergrowth having the spinel (111) planes as the interface. As several equivalent (111) planes, forming an angle equal to 70°, coexist in the spinel structure, twinned intergrowth could be observed in some crystals. Such a twinning is presented in Fig. 6b where the contrast change attributed to the intergrowth is observed along two directions.

Nevertheless, these observations did not allow identification of the new phase.

(6) $Li_{0.1}Mn_2O_4$ Sample

(a) SAED study. SAED study on the d^1 sample ($Li_{0.1}Mn_2O_4$) was carried out on numerous crystallites. All of them exhibited bi-(or tri-) phasic patterns. In these patterns, the spinel reflections (with lower intensities than before), the "distorted low-symmetry spinel" reflections, as well as diffuse lines along all equivalent $[111]_{(S)}$ directions (whose intensities are reinforced) are still observed besides new intense spots. The reconstruction of the reciprocal space showed that they belong to a unique phase with hexagonal cell parameters ($a \approx 5.8$ Å, $c \approx 8.9$ Å). The observed growth process together with these parameter values directed us toward a spinel–double hexagonal phase transition. Indeed, these parameters values are consistent with the known $LiFeSnO_4$ DH type cell parameters although slightly smaller. Such a difference can be accounted for by the cation size difference (octahedral Mn^{4+} ($r = 0.67$ Å) being significantly smaller than Fe^{3+} (0.785 Å) and Sn^{4+} (0.83 Å) (19)). In addition, the tetrahedral lithium occupancy is equal to 1 in $LiFeSnO_4$ while it should be lower in the Li–Mn–O as addressed below. Moreover, from the SAED patterns, the reflection condition for the new phase is $hh\bar{2}hl$ ($l = 2n$), leading to $P6_3/mmc$ or $P6_3mc$ space groups identical to DH space group. The ex-$[111]_{(S)}$, $[1\bar{1}0]_{(S)}$, and $[11\bar{2}]_{(S)}$ SAED patterns are given in Figs. 7a, 7b, and 7c, respectively.

Although the final product cannot be considered as monophasic, the topotactic character of the transformation is easily established from these SAED patterns through the

TABLE 1

Sample name	Chemical composition	X-ray observation	TEM observation
a^1	Stoichiometric $LiMn_2O_4$	Pure spinel phase	Pure spinel phase, no representative faults
b^1	$Li_{0.9}Mn_2O_4$	Growth of extra peak; 19.415° ($d = 4.57$ Å), 21.84° ($d = 4.07$ Å), 37.06° ($d = 2.43$ Å) and 43.61° ($d = 2.08$ Å); extra reflections; spinel peaks become broader	Nucleation of the new phase in the form of staking faults in the $[111]_{(S)}$ layers
c^1	$Li_{0.5}Mn_2O_4$	Growth of extra peaks; displacement of all the reflections toward high angles; a third peak at 18.3° ($d = 4.8$ Å); emerges from the spinel reflection foot	Intergrowth of the new phase in the spinel matrix; planar growth along $[111]_{(S)}$ layers; nucleation starts along all equivalent $[111]_{(S)}$
d^1	$Li_{0.1}Mn_2O_4$	Numerous extra reflections now observed; spinel reflections still moving toward high angles	Identification of the new phase as isotypic with a DH phase; crystallographic relationships between DH and spinel were established by TEM; high-resolution observation of the crystal evidences size of spinel, DH, and intermediary domains
e^1	$Li_{0.85}Mn_2O_4$	All extra reflections vanish with relithiation of the sample; spinel reflections convert back to their initial position with a slight width increase	All the DH intergrowth domains, most of the stacking faults, as well as large disordered interfaces disappear, proving the reversibility of the transition
f^{80}		Fully lithiated sample obtained after 80 cycles; broadening of the spinel reflections carries on, indicating an increase of strains in the particles	More and more remaining stacking faults are observed inside the particles
g^{80}		fully delithiated sample obtained on an oxyfation following the 80th cycle; spinel reflections indicate a pseudo-amorphization of the intensity of extra reflections does not increase	The size of DH domains does not increase while amorphization increases inside other domains

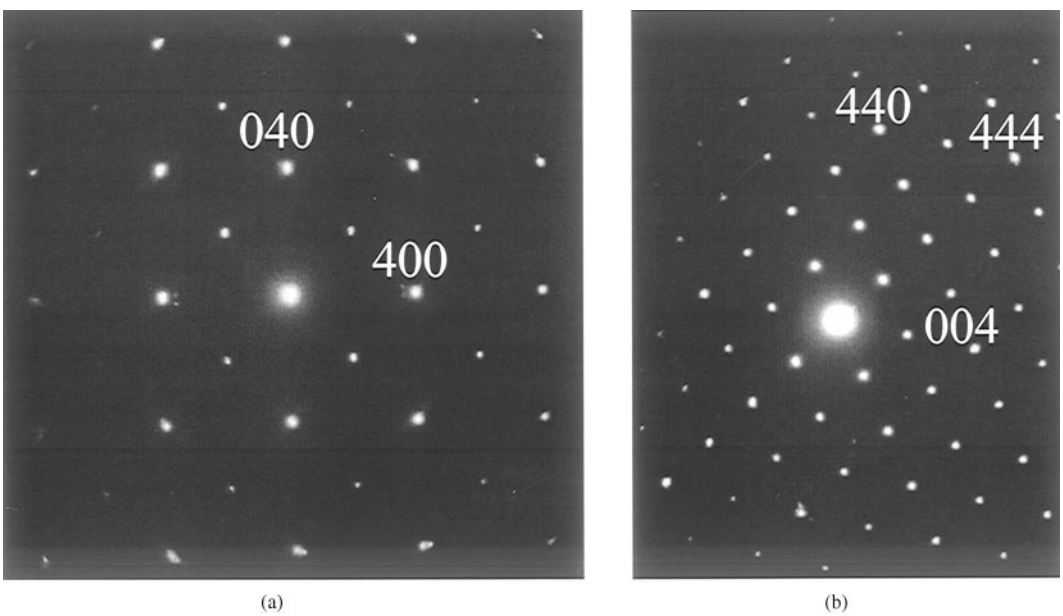

FIG. 4. Experimental SAED patterns realized on the starting $LiMn_2O_4$ (a^1 sample) material, (a) along the [001] zone axis and (b) along the $[1\bar{1}0]$ zone axis.

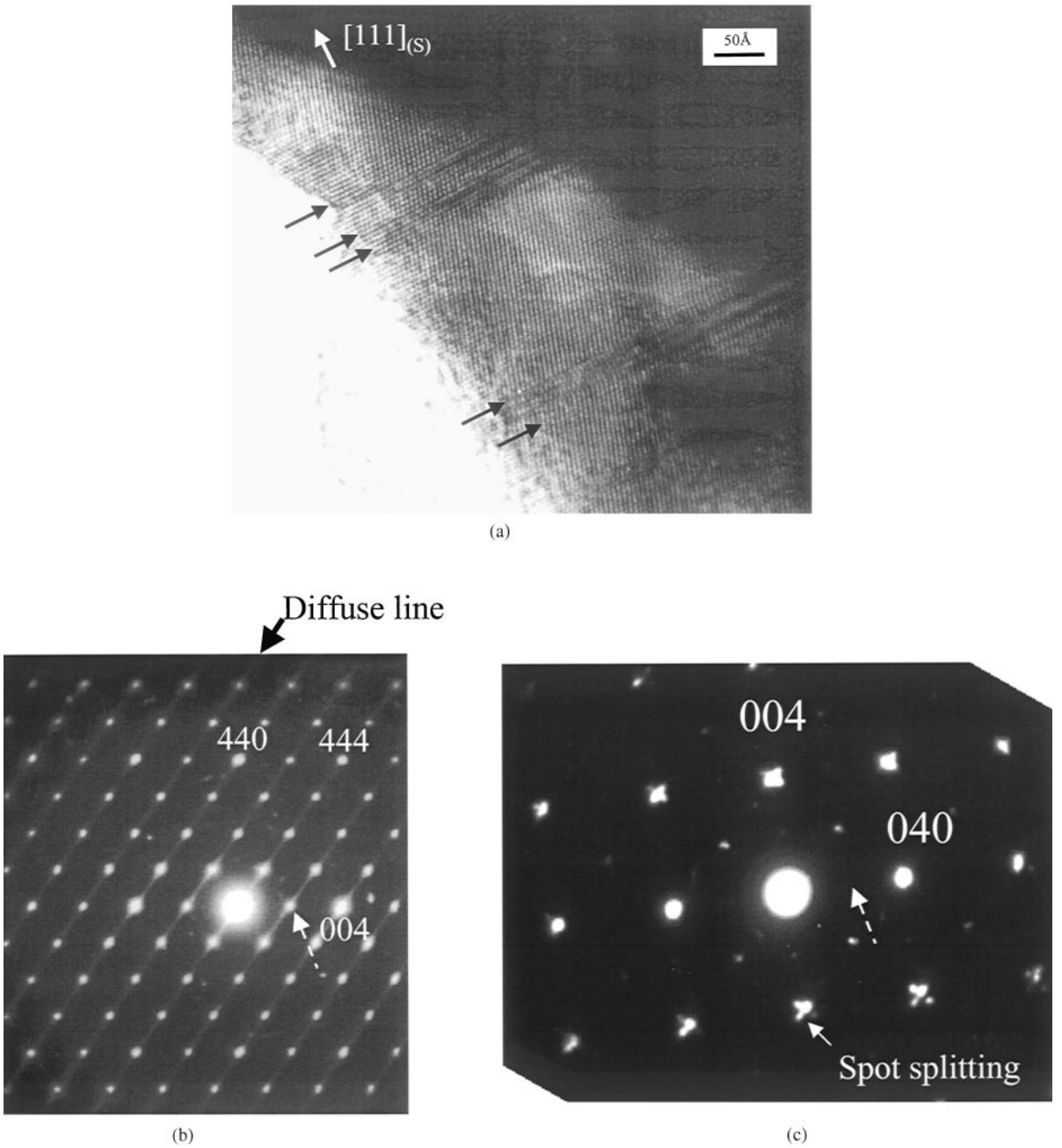

FIG. 5. (a) Bright field image realized on $Li_{0.9}Mn_2O_4$ (b^1) sample showing stacking faults denoted by black arrows. SAED patterns realized on the same crystal (b) along [100] and (c) along $[1\bar{1}0]$; the dashed white arrows refers to forbidden reflections for the spinel structure, the plain black arrow shows the direction of the diffuse lines ([111]* direction).

observed crystallographic relationship between spinel and DH. Thus, the three following relationships were determined and verified along the previously presented zone axis: $[111]_{(S)}//[001]_{(DH)}$ (Fig. 7a); $[1\bar{1}0]_{(S)}//[110]_{(DH)}$ (Fig. 7b); $[11\bar{2}]_{(S)}//[1\bar{1}0]_{(DH)}$ (Fig. 7c).

(b) The double hexagonal type structure hypothesis. The validity of the spine–DH phase transition hypothesis can consequently be discussed by comparing the collected TEM/SAED images and patterns and the geometrical consideration proposed by Choisnet *et al.* (13). First, the use of kagome and Te_2Oc layers as bricks to describe both structures fit well with the bright field observations and the $[111]_{(S)}//[001]_{(DH)}$ relationship. Indeed, both spinel and DH are built with similar layers stacked along a common direction ($[111]_S$ or $[001]_{DH}$) and the (111) spinel planes should

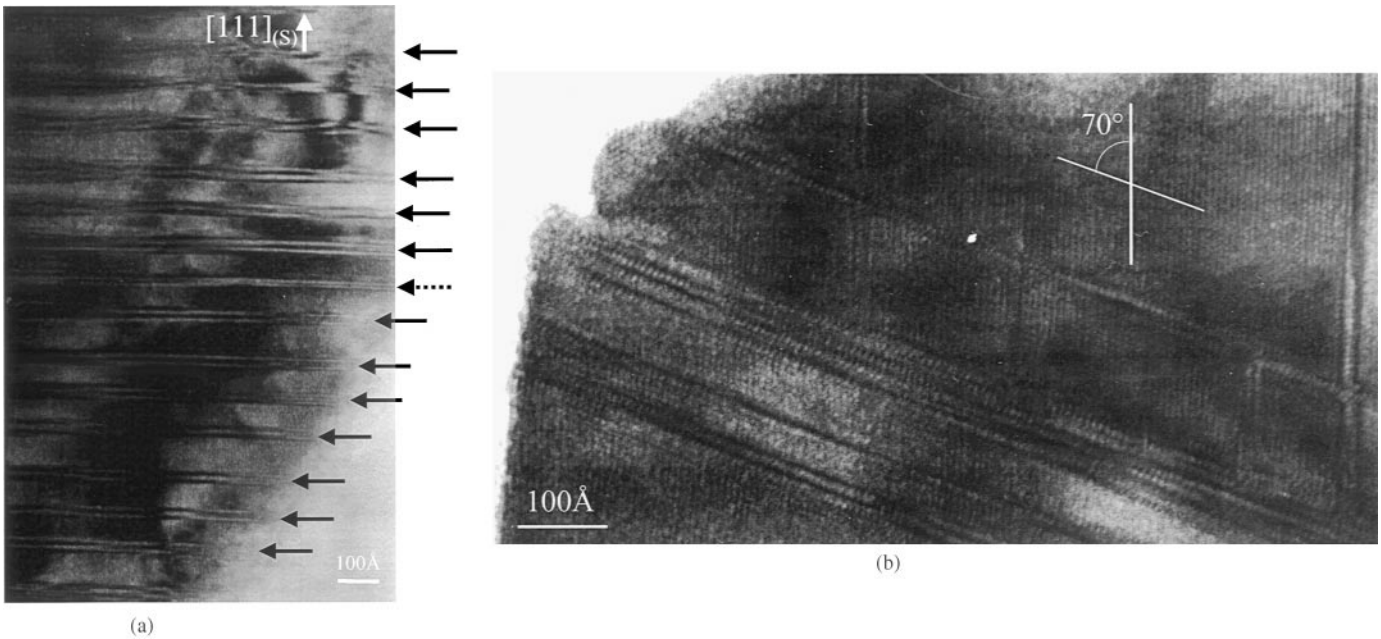

FIG. 6. Bright field image realized along $[1\bar{1}0]_S$ showing (a) the planar growth of the faults (plain and dashed black arrows for intergrowth domain thickness equal to 27 Å and 14 Å, respectively) and (b) twinning of the intergrowth occurring along two equivalent $[111]_S$ directions forming an angle of 70° as reported on the image.

act as the nucleation and growth interfaces since the energy required for the transformation will be minimum when the above relationships are satisfied. Identically, if the implied structures are drawn along the directions corresponding to the two other sets of relationships ($[\bar{1}10]_{(S)}//[110]_{(DH)}$), and $[11\bar{2}]_{(S)}//[1\bar{1}0]_{(DH)}$), the similarity between each pair of representations is obvious.

Two mechanisms could be proposed to explain the sliding of the layers: a local process using only two consecutive oxygen layers or a global process using the concerted displacement, in one step, of a part of the crystal sliding on the other part of the crystal. The first mechanism could be retained, according to the TEM bright field images recorded during the nucleation (Fig. 5a) as well as the growth first stage (Figs. 6a, 6b), which illustrate perfectly this progressive mechanism. The monitoring of two layers, which have started to slide (black arrows), reveals that while the transformation is effective on a part of the layers, the other part is still unaffected (Fig. 5a). Moreover, from an energetic point of view, the transformation should be easier by progressive sliding of two consecutive oxygen layers (soft transition, possibilities for the crystal to relax strains) than by sliding of a large block of matter (concerted transformation, large interface, uncommon mechanism in a solid-state transformation). We will discuss later, from a structural point of view, the needs and consequences of such a mechanism on our material.

This structural information has facilitated the interpretation of the $Li_{0.1}Mn_2O_4$ powder pattern.

(c) X-ray diffraction study. The phase assignment of the observed X-ray reflections is reported in Fig. 8 and the indexing in Table 2. The S and DH symbols refer to the refined spinel cell ($a = 8.05(2)$ Å, $Fd\bar{3}\,m$), and the double hexagonal cell ($a = 5.74(2)$ Å, $c = 8.93(2)$ Å, $P6_3mc$), respectively. It is worth noting that the quality of the cell refinement is poor for the double hexagonal phase, and that weak broad extra reflections are still nonindexed. The corresponding inter-reticular distances for the weak reflections reveal a relationship with the spinel cell. For instance, the weak reflection at $d = 4$ Å could be indexed as a theoretically forbidden 200 spinel reflection. This remark could be generalized to other weak reflections, and consequently this entire set of peaks could be ascribed to a "distorted spinel cell" denoted DS, described as an average cubic cell ($a = 8.08(2)$ Å $Pm\bar{3}m$) undergoing a severe symmetry loss. The HREM section will focus on the reality of this "distortion".

Regarding the poor quality of the DH phase refinement due to small and badly crystallized domains, we believe it is due to the fact that although the lithium deintercalation is nearly complete, the phase transition is not. This remark is consistent with the observed SAED patterns that have revealed diffuse lines (Figs. 7b, 7c) and still the presence of a spinel phase (Figs. 7a–7c) implying that the layer stacking mode is not affected or is partially affected by the phase transition. According to the enhancement of diffuse line intensities (comparison of Figs. 5b and 7b), numerous large stacking faults are now scattered in the crystal and affect all

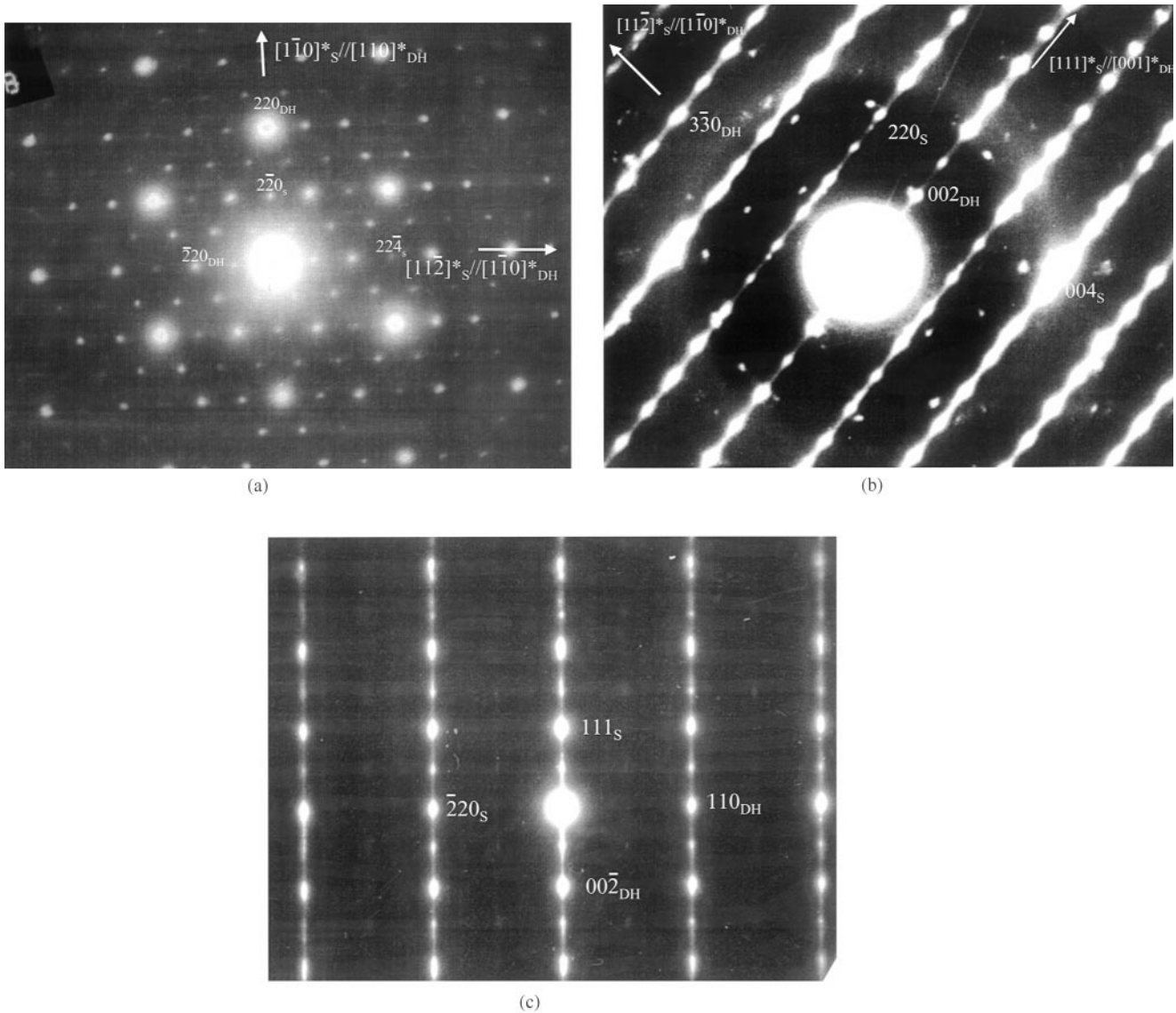

FIG. 7. Experimental SAED pattern realized on $Li_{0.1}Mn_2O_4$ (d^1 sample) showing the crystallographic relationships between DH and spinel phases: (a) $[111]_{(S)}//[001]_{(DH)}$ zone axis; (b) $[1\bar{1}0]_{(S)}//[110]_{(DH)}$ zone axis; (c) $[11\bar{2}]_{(S)}//[1\bar{1}0]_{(DH)}$ zone axis.

the $[111]_S$ equivalent directions (Fig. 6b). The spinel–DH transition should occur anywhere in the crystal and the interfaces become pinned, leaving non-fully transformed domains keeping a spinel type structure and having the λ-MnO_2 composition ($Li_\varepsilon Mn_2O_4$ to be exact).

(d) HRTEM study. (1) Observations realized on HRTEM images. As deduced previously from SAED and bright field image results, one of the best orientations for characterizing the phases and then the transformation mechanism is the $[1\bar{1}0]_{(S)}$ direction. Along this zone axis, the atoms building the kagome and Te_2Oc layers form atomic columns projecting over the same point on the $(1\bar{1}0)$ plane (Figs. 1e, 1f), thereby directly revealing the stacking sequence along $[111]_S$. As reported above, the two phases could be differentiated by their oxygen close-packing sequences and packing type. Spinel structure presents an ABC oxygen layer sequence corresponding to only cubic (denoted c) type packing (… cccc …) while DH structure shows an ABAC oxygen layer sequence corresponding to alternation of cubic and hexagonal (h) type packing (… chch …).

A parallel could be drawn with the stacking sequences observed in hexagonal perovskites. A method of describing the AMX_3 perovskite structure is based on the stacking of AX_3 layers. The stacking of these layers is of the cubic type and M cations occupy the octahedral cavities. This description is useful in understanding hexagonal polytypes, which correspond to different percentages of cubic and hexagonal

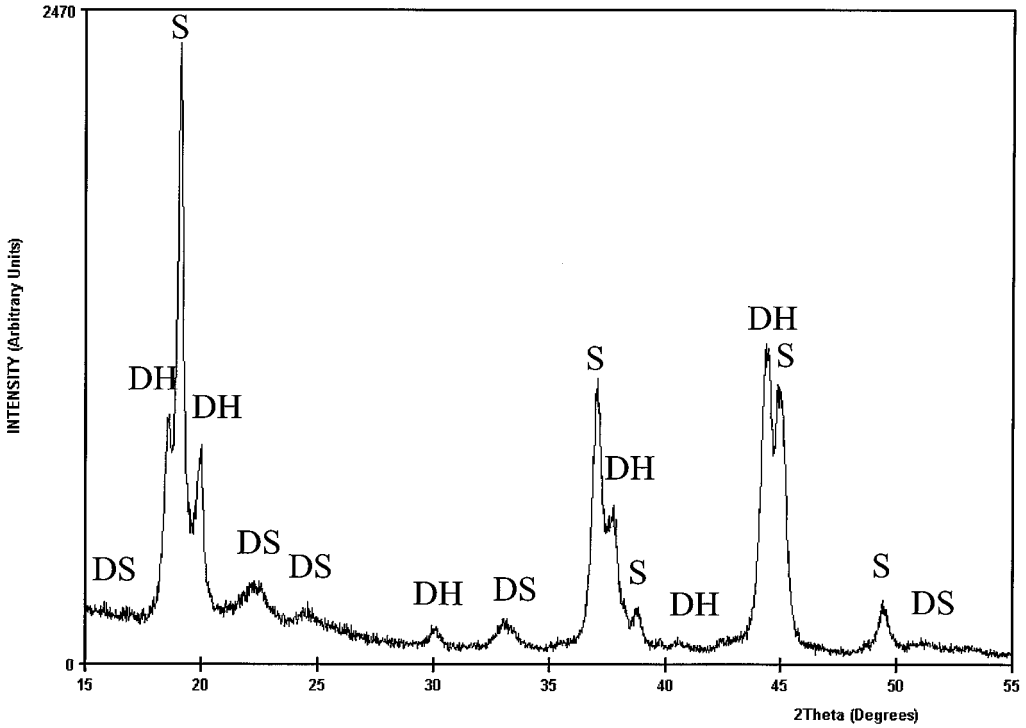

FIG. 8. Powder X-ray diffraction pattern realized on d^1 sample obtained after the first oxidation up to the nominal composition $Li_{0.1}Mn_2O_4$ and indexed using DH, double hexagonal cell ($a = 5.74(2)$ Å, $c = 8.93(2)$ Å, $P6_3mc$); S, spinel cell ($a = 8.05(2)$ Å, $Fd\bar{3}m$); DS, distorted spinel cell ($a = 8.08(2)$ Å, $Pm\bar{3}m$).

stacking (20). For a long time, in these systems, HRTEM has been used to obtain easily the implied perovskite type structures (21–23). Indeed, on the HRTEM images the hexagonal close-packed stacking will induce observation of a chevron type contrast. Each observed chevron indicates a hexagonal close-packed arrangement of the associated oxygens and makes it possible to determine the stacking sequence directly from an image. It is worth noting that contrast from the lower resolution bright field image is also sensitive to changes in the stacking sequence.

TABLE 2

2θ (°)	d (Å)	Indexation using the spinel unit cell $a = 8.05(2)$ Å, $Fd\bar{3}m$	Indexation using the "distorted" spinel unit cell $Pm\bar{3}m$	Indexation using the double hexagonal unit cell $a = 5.74(2)$ Å, $c = 8.93(2)$ Å, $P6_3mc$
15.6	5.7		110	
18.5	4.8			100
19.0	4.6	111	111	
20.0	4.4			002
22.1	4		200	
24.7	3.6		210	
31.0	2.9	220	220	110
33.2	2.7		300	
37.1	2.4	311	311	
37.7	2.38			201
38.9	2.3	222	222	
40.6	2.2		320	
44.4	2.04			104
44.9	2.02	400	400	
49.4	1.8	331	331	

For our spinel–DH system, this last point was illustrated by the bright field images (Figs. 5c, 6a, 6b) observed during the nucleation and intergrowth process. [$1\bar{1}0$] HRTEM images and the corresponding SAED pattern are given in Figs. 9a–9d. At Scherzer defocus, the high electron density zones appear in black. Consequently, the manganese atoms (large spheres in Fig. 1) will give the black dot array forming the contrast. The ABC spinel stacking will induce a contrast formed by individual dots forming parallel lines tilted by 70° versus the (111) planes (the created motif is a flattened hexagon circled in Fig. 1e) while the ABAC double hexagonal structure will induce a "wavy" contrast parallel to the $[001]_{DH}$ direction (corresponding to the waves noted in Fig. 1f). These two types of contrasts could be identified on the images.

In the thinnest part of the crystal, changes in the [111] layer stacking are observed. Consecutive cubic close packing is limited to a few atomic layers (noted … ccccc …) in small 20 Å bands (Fig. 9b, domain surrounded by the white

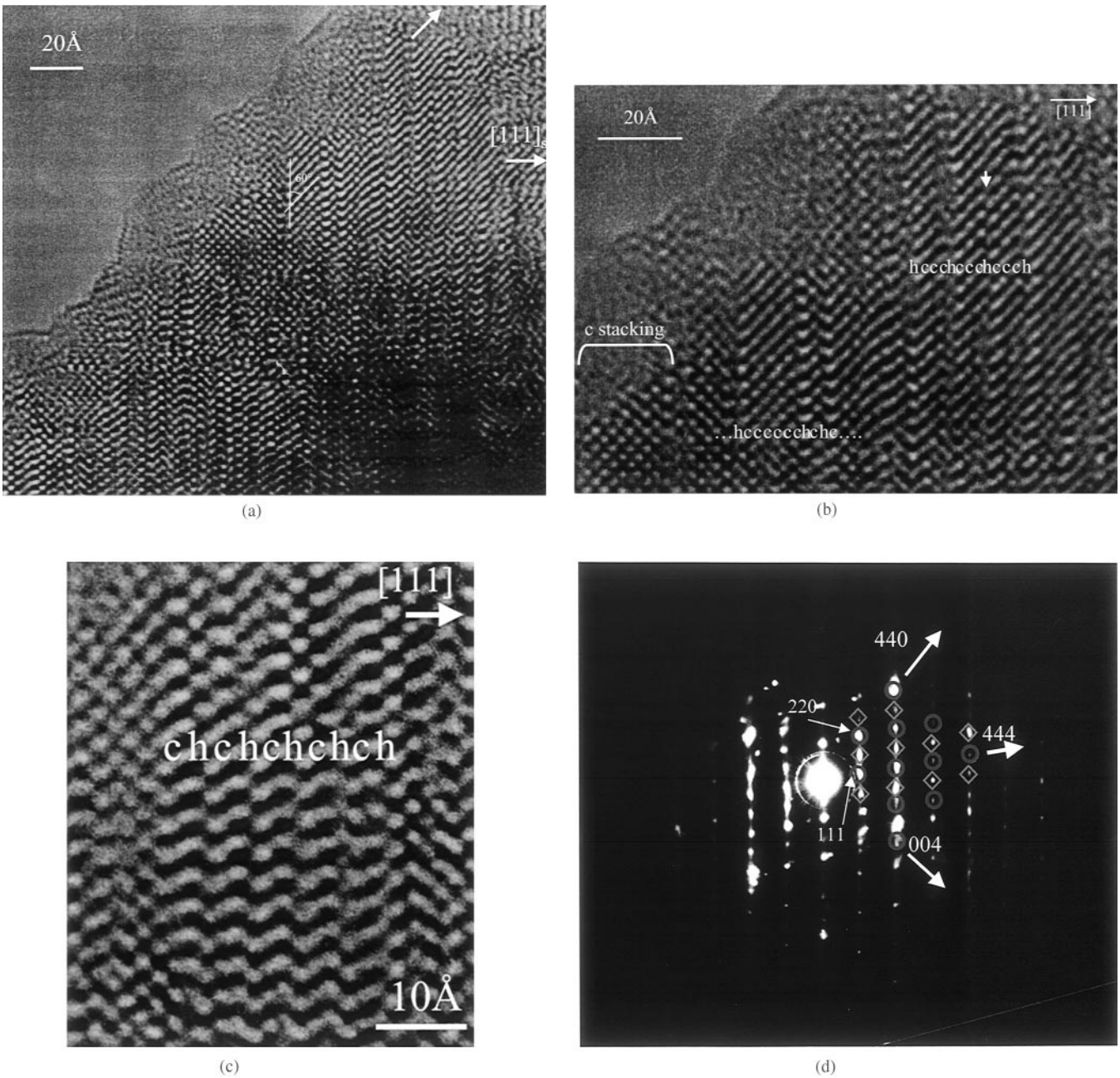

FIG. 9. (a) Overall high-resolution electron microscopy image realized on d^1 sample ($Li_{0.1}Mn_2O_4$ nominal composition) along $[1\bar{1}0]$ where messy domains could be observed; bold white arrows point the "equivalent" $[111]_S$ direction. (b) Enlarged image showing a "large" region (delimited by a white bracket) where cubic stacking (… ccccccccc …) contrast could be identified and other regions where random hexagonal stacking (denoted h) are observed. The white arrow points to a sliding of layers in progress: under the arrow the layer staking is hexagonal while above it the stacking is cubic. (c) Enlarged image showing a region where (… chchchchch …) sequence, corresponding to the DH layer stacking, is observed. Note, by grazing incidence, the variation in the layer spacing. (d) Corresponding SAED pattern where strong distortion of the spinel subcell as well as twinning is observed. The circled spots could be indexed with the spinel cell ($a = 8.05(2)$ Å, $Fd\bar{3}m$), while the ones framed with lozenges are induced by the strong distortion, twinning, and double hexagonal domains creation.

bracket). On another part of the crystal (Fig. 9c), wavy contrast attributed to the DH phase and fitting perfectly with the (chch) sequence is observed. The width of theses DH domains is mainly equal to 12 layers corresponding to 27 Å. Apart from these two types of well-defined contrasts, the rest of the contrast forming the crystal image is composed of randomly distributed zigzags. The chevron sizes and periodicity (as noted in Fig. 9b) are different from one

another, indicating that the corresponding hexagonal close packing should be considered as stacking faults in the initial cubic type packing. Viewing the overall and enlarged pictures at grazing incidence along either one of the $[111]_S$ directions (bold white arrows) or along the (111) planes clearly shows variation in the layer spacing corresponding to (111) inter-reticular distance variations and inducing the incommensurable modulation of black and white dot rows. Moreover, in the assumed spinel domains (white bracket in Fig. 9b), the angle measured between the equivalent $[111]_S$ directions varies from one crystallite to another. Most of them, close to 60°, are quite different from the expected 70°. The heaping of layers could not then be interpreted in terms of pure ABC or ABAC stacking (since an equivalent position could not be found after x stacks) but rather attributed to an "intermediate" stacking stage induced by partial layers sliding perpendicularly to the [111] direction. These shifts, not self-connected, bring out the random messy stacking observed on some domains. Such an empirical stacking is responsible for the distorted spinel mentioned in the X-ray study.

From a crystallographic point of view, the "distorted" spinel could not then be considered as a fully extra phase with well-defined parameters and atomic positions. It corresponds to an entity encompassing all the domains where spinel or DH stacking descriptions could not be used. The mechanism being not self-connected, blocking interfaces are formed leading to this observed incomplete transformation. Moreover, these observations are consistent with the assumed phase transition model, which involves the sliding of two consecutive rows of oxygen. To be able to move locally and to propagate, the oxygen layer sliding requires the departure of lithium atoms captive in the tetrahedral site. The understanding of this point is essential to the transition mechanism presented below.

(2) Observations on corresponding SAED pattern. Using the corresponding SAED pattern (Fig. 9d), additional information such as the average parameters of the cell building the distorted domains could be extracted. The spinel phase contribution in terms of spots is circled in blue in Fig. 9d. The presence of the 002 spot reveals the symmetry loss and other extra spots are framed in a lozenge. This second set of reflections could be deduced from the first one with a twinning using the two equivalent [111] directions (the (111) plane acting as a mirror). d spacing calculations evidence the strong distortion of the spinel cell: for instance, the (004), (220), and (111) inter-reticular distances are measured to be equal to 2.00 Å, 2.87 Å, and 4.72 Å, respectively (for comparison, the equivalent distances for λ-MnO_2 are 2.01, 2.84, and 4.64Å).

Assuming that this strong distortion could be associated with an intermediate step between λ-$Li_\varepsilon MnO_2$ ($a = 8.05$ Å) and DH phases ($a = 5.74$ Å, $c = 8.93$ Å) and using the measured distances, a cell (monoclinic or triclinic) could be calculated. The measured γ angle is close to 60° and average reciprocal parameters are close to $a^* = (1/a \sin\gamma) \approx b^* \approx 4.94$ Å^{-1}. The c parameter was calculated using the distance measured along [111] and the number of slices composing the spinel and double hexagonal cells (corresponding c axis). Figures 1e and 1f show that spinel is formed with six slices instead of four for the DH phase. By geometrical considerations, then, the common repeat corresponding to the intermediate monoclinic "mixed" cell will contain 12 slices (multiple of 6 and 4). In the spinel cell, the six layers stack along the cube diagonal, and the slice thickness is equal to $a\sqrt{3}/6 \approx 2.3$ Å (using an average a parameter of 8.1 Å). The overall result is then a monoclinic c parameter of about 27 Å.

(3) Measured distances and periodicity interpretation. This last value of 27 Å is recurrent. It corresponds to the average width of the pure DH domains as well as the spacing of the black lines delimiting the hexagonal stacking faults (intergrowth) observed in the spinel matrix during the nucleation/growth first stage. Since the common periodicity for spinel and DH is equal to 12 layers, it is natural that the perfect DH stacking domains grow inside spinel with a width equal to a multiple of 27 Å. During the nucleation/first stage of growth steps (Section 4), the 27 Å repeat (with some 14 Å repeat) of the black lines observed on the bright field images could be linked to the creation of the early hexagonal type stacking in the cubic stacking matrix. In terms of close-packed oxygen stacking, the insertion of a hexagonal stacking in the ABCABC cubic sequence (i.e., cccccc) will induce the formation of an ABACBC sequence by sliding two consecutive oxygen layers. The translation in c and h terms is (chcchc). Six layers are implied during the formation of the early hexagonal stacking which correspond to the $6 \times 2.3 \approx 14$ Å distance observed on the bright field image (Fig. 6). The sliding and stacking change of oxygen layers should induce strains inside the material. The minimization of theses strains could occur by the creation of two inverse sets of oxygen layers sliding to annihilate (at least partially) the strains. The presence of such mirrors is well known in hexagonal perovskite and is responsible for the zigzag contrast (20). In the spinel–DH system, 12 layers are necessary to obtain sliding inversion. Starting with ABCABCABCABC stacking (c type stacking), ABACABCABACABC stacking could be proposed and could lead to (chch)cccc(hchc) stacking. The corresponding calculated repeat distance fit well with the 27 Å mainly measured on the images. Moveover, in opposition with the previous chcchc sequence, the (chch)cccc(hchc) sequence holds already two perfect sequences chch, of the DH phase. Another way to minimize the strains is to space out the nucleation region. The measured internucleation region spacing ranges between 81 and 110 Å (i.e., between 3 and 4 times 27 Å). This

spacing should be sufficient for a dissipation of the strain inside the spinel domains. When this minimum spacing will no longer be respected due to an increasing number of hexagonal faults (as found for the $Li_{0.1}Mn_2O_4$ sample in the HREM part), only a distortion of the spinel cells will allow a partial dissipation of the strains. Finally, the strains inside the materials as well as the large distance between two nucleation domains will go against a complete transformation of the spinel into DH phase by creation of stacking misfits and exotic interfaces.

(7) Reversibility of the Phase Transition, the Samples Obtained after the First and 80th Cycle

The previous sample (sample d^1) is reduced to 3 V to give the e^1 sample (nominal composition $Li_{0.85}Mn_2O_4$). X-ray diffraction realized on this reduced sample clearly evidences a pure spinel pattern. The cell refinement ($a = 8.234(1)$ Å, $Fd\bar{3}m$) is in good agreement with the parameter considered for a spinel with such a lithium content. Nevertheless a doubling of the full width at half-maximum (FWHM) of the peaks together with a broadening of each reflection foot are observed for the cycled material compared to the starting material. Such features are enhanced upon subsequent cycles. A broadening of the peaks is often ascribed to a crystallite size decrease, a crystal strain enhancement, or both. This point was confirmed by TEM observations with namely the presence of a few stacking faults remaining in the reduced samples, as shown in Fig. 10. This micrograph evidences the few remaining stacking faults (black dashed arrows), along the $[111]_S$ direction, observed in a representative particle of the sample obtained after one full cycle. Are these faults responsible for the irreversibility (17%) measured on the electrochemical curve during the first cycle? According to the chemical formula, and assuming that these faults could not accommodate lithium insertion, they should indeed represent 17% of the material and thus we believe them to be responsible for the irreversible capacity loss observed after the first cycle. After 80 cycles, the reversibility is conserved (Figs. 3f, 3g). The spinel reflections became broader and broader while DH reflections do not seem to be affected by this degradation. The X-ray diffraction analysis (intensity and FWHM of peaks) shows that, from the structural point of view, the DH crystallinity and crystallite size do not change. This result is consistent with the observed high capacity retention of the 3.3/3.95 and 4.5 V anomalies upon cycling.

(8) Correlation between Structural and Electrochemical Results

Attempts to correlate all of these structural results with the electrochemical ones (8) in light of the previously schematic model (8) are now presented. We showed that as soon as the lithium starts leaving the spinel host structure, a well-defined oxidation level of 3.95 V and nucleation of the new DH phase begin locally by displacement of two consecutive oxygen layers. Due to the low amount of nucleus, the DH phase domains can expand easily since the strains are not yet significant. These new phase domains propagate in the spinel particle by a progressive sliding of the implied layers and consequently by following the spinel (111) planes as interfaces. Our previous paper (8) showed that the creation of a DH phase requires the extraction of half of the lithium to allow the migration of oxygen and manganese from one site to another. This value is consistent with the gliding of the layers described in this paper: the spinel–DH phase transition requires the transformation of a K/T junction to a K/O junction. The lithium blocking the kagome window should be removed before the oxygen and manganese migrate. Consequently the DH phase formed should have a $Li_{0.5}Mn_2O_4$ chemical composition. Based on the observation that a sample partially oxidized to $x = 0.5$ "$Li_{0.5}Mn_2O_4$" and reduced to 3 V shows the same capacity as a sample fully oxidized and reduced, we conclude that the maximum amount of the "real" DH phase is already obtained when 0.5 lithium is extracted from the $LiMn_2O_4$ battery electrode. It is worth mentioning as experimentally deduced that this amount of DH phase represents only 30% of the sample. Upon further delithiation (0.5 to 0.8 lithium removed from the sample), we observed that local structural

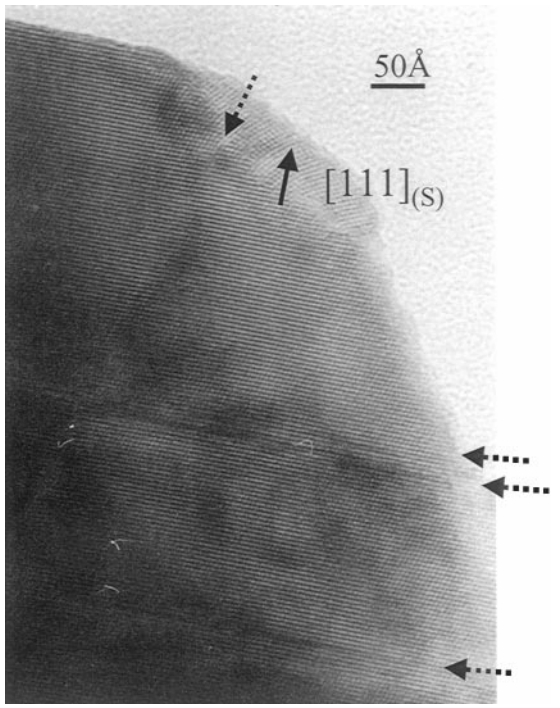

FIG. 10. Bright field image realized along $[1\bar{1}0]_S$ on e^1 sample obtained after one full electrochemical cycle and showing the few remaining faults (dashed arrows) responsible for the slight broadening of the spinel reflection on the corresponding X-ray diffraction pattern (Fig. 3e).

layer rearrangements continue. Therefore, the increasing number of stacking faults does not favor the formation of a perfect DH type layer stacking. Only partial and messy spinel transformation occurs in these domains due to constraints (twinning) and misfits of several reorganizations having different starting points. For these so-obtained messy domains the extraction of the second half of the lithium starts (potential at 4.1 V on the electrochemical curve). When 0.8 lithium is extracted from the sample, almost only the lithium trapped in the well-crystallized DH phase (30% of the material) remains. These lithium atoms then leave this structure, showing a characteristic signature at 4.5 V (the extra plateau). Once fully oxidized, the sample is reduced, and the mechanism inverts itself. Lithium is first inserted inside the 30% of the DH host up to a limit composition equal to "$Li_{0.5}Mn_2O_4$" for these domains. The filling of the distorted spinel then takes place with a renewal of symmetry in the cells building these messy domains up to classical cubic spinel phase parameters and symmetry. Finally, the insertion of more lithium in the $Li_{0.5}Mn_2O_4$ DH domains causes the phase transition to spinel characterized by a well-defined reduction peak at 3.3 V (8).

This mechanism then explains why the two extra plateaus are linked one to another and have the same electrochemical capacity. Nevertheless, TEM results showed that the types of transition inducing these steps are quite different. The 4.5 V plateau is due to a delithiation following the solid solution rule (high kinetics and no hysteresis). The host framework is the same, except the DH composition changes continuously from "$Li_{0.5}Mn_2O_4$" to "MnO_2." In contrast, the 3.3 V plateau corresponds to a reconstructive phase transition implying a strong structural changes from DH structure to spinel structure then explaining the 650 mV drop in potential (Fig. 2).

It is worth noting (Fig. 2) that irreversibility is high for the first cycle and continuous capacity fade takes place upon cycling. This capacity fading seems to be exclusively due to the spinel domains, as the capacity on the 4.5 V and 3.3/3.95 V steps remains constant upon cycling. Such an observed effect could be correlated with the subsisting faults in the spinel particle observed after full reduction and with the broadening of the spinel reflections. These reflections indicate a decrease in the crystallite size and, conversely, an increase of the crystallite joint number. These joints and faults should lock some lithium sites, preventing further Li insertion. Nevertheless, it seems that they are not sufficient in number to explain an irreversibility of 0.2 lithium.

This study has clarified that the origins of the additional 3.3/3.95 and 4.5 V redox peaks observed in some $LiMn_2O_4$ are rooted in a cubic–DH phase transition; however, no clues were obtained regarding this phase transition driving force. In a parallel study a survey on the effect of various parameters such as the nature of the precursors (amorphous vs crystallized or faulted), the annealing temperature, the ambient atmosphere, and others on the appearance of the 3.3 and 4.5 V redox peaks was pursued. The universal trend was that the signature of these anomalies was appearing on samples having cell parameters greater than 8.24 Å (e.g., large volume). Thus, could such a phase transition be a volume-driven phase instability (compacity of the spinel phase being smaller than that of the DH one) as suggested by Choisnet *et al.*, in the $Li_2Cr_{3-x}Fe_xSbO_8$ antimonate system and its derivatives?

CONCLUSION

For the first time, the phase transition responsible for the two extra plateaus at 4.5 and 3.3/3.95 V observed on "abnormal" spinel voltamograms was identified by means of TEM studies. Theses steps are the signatures of a lithium manganese oxide having a double-hexagonal type structure. The first plateau at 3.95 V observed during the charge corresponds to the spinel-to-double hexagonal phase transition. During this transformation, half of the lithium blocking the kagome windows should be removed before other atoms migrate. The assumed chemical composition of the so-formed DH phase is $Li_{0.5}Mn_2O_4$. Upon further delithiation, the remaining half of the lithium, contained in the DH structure, leaves the host without structural changes, showing a characteristic signature at 4.5 V on the voltamogramm. During the following discharge, this latter process is perfectly reversible as evidenced by the plateau observed at 4.5 V. Upon further lithiation, the DH phase then transforms back to the spinel phase. This transition is characterized by a well-defined plateau observed at 3.3 V on the electrochemical curve. The efficiency of the electrochemical route to synthesize this double hexagonal phase is poor since less than 30% of the spinel particle "perfectly" transforms into double hexagonal. The remaining volume is formed of domains where the transformation is incomplete, and where messy stackings of atoms layers are observed. Using TEM results, all the reflections observed on the corresponding powder X-ray diffraction patterns were attributed either to spinel ($a = 8.05(2)$ Å $Fd\bar{3}m$), distorted spinel ($a = 8.08(2)$ Å, $Pm\bar{3}m$) or double hexagonal ($a = 5.74(2)$ Å, $c = 8.93(2)$ Å, $P6_3mc$) phases.

Also, of this study shows that the pure lithium manganese DH phase cannot be obtained by the electrochemical method. Several cycles as well as kinetic effects are useless to increase the percentage of synthesized DH phase.

We presently are investigating cation-driven volume changes in stannide compounds with the hope of isolating compounds having a 100% bulk cubic–DH transition.

ACKNOWLEDGMENTS

We acknowledge the support of the Ministerio de Educación y Cultura (Spain) and the Ministère de l'Education Nationale de la Recherche et de

la Technologie (France) in the framework of a French-Spanish Picasso program.

REFERENCES

1. Y. Gao and J. R. Dahn, *J. Electrochem. Soc.* **143**(1), 100 (1996).
2. G. G. Amatucci, C. N. Schmutz, A. Blyr, C. Sigala, A. S. Gozdz, D. Larcher, and J. M. Tarascon, *J. Power Sources* **69**(1–2), 11 (1997).
3. Y. Gao and J. R. Dahn, *Solid State Ionics* **84,** 33 (1996).
4. J. M. Tarascon, W. R. McKinnon, F. Coowar, T. N. Bowmer, G. Amatucci, and D. Guyomard, *J. Electrochem. Soc.* **141**(6), 1421 (1994); *Phys. Condens. Matter* **9,** 1729 (1997).
5. M. Tabuchi, C. Masquelier, H. Kobayashi, R. Kanno, Y. Kobayashi, T. Akai, T. Maki, H. Kageyama, and O. Nakamura, *J. Power Sources* **68,** 623 (1997).
6. M. R. Palacín, G. G. Amatucci, M. Anne, Y. Chabre, L. Seguin, P. Strobel, J. M. Tarascon, and G. Vaughan, *J. Power Sources* **81–82,** 627 (1999).
7. A. Mosbah, A. Verbaere, and M. Tounoux, *Mater. Res. Bull.* **18,** 1375 (1983).
8. M. R. Palacín, Y. Chabre, L. Dupont, M. Hervieu, P. Strobel, G. Rousse, C. Masquelier, M. Anne, G. G. Amatucci, and J. M. Tarascon, *J. Electrochem. Soc.* **147**(3), 845 (2000).
9. G. Rousse, C. Masquelier, J. Rodríguez-Carvajal, and M. Hervieu, *Electrochem. Solid State Lett.* **2**(1), 6 (1999).
10. A. Yamada and M. Tanaka, *Mater. Res. Bull.* **30**(6), 715 (1995).
11. A. Yamada, *J. Solid State Chem.* **122,** 160 (1996).
12. J. Choisnet, M. Hervieu, B. Raveau, and P. Tarte, *J. Solid State Chem.* **40,** 344 (1981).
13. J. Choisnet, M. Hervieu, B. Raveau, and P. Tarte, *J. Solid State Chem.* **45,** 280 (1982).
14. S. Iida, *J. Phys. Soc. Jpn.* **12,** 222 (1957).
15. F. Le Cras, P. Strobel, M. Anne, D. Bloch, J. B. Soupart, and J. C. Rousche, Eur. *J. Solid State Inorg. Chem.* **33,** 67 (1996).
16. D. Guyomard and J. M. Tarascon, *J. Electrochem. Soc.* **139**(4), 937 (1992).
17. J. Rodriguez-Carvajal, *in* "Collected abstracts of powder diffraction meeting," Toulouse, France, July 1990 (J. Galy, Ed.), p. 127.
18. K. Yvon, W. Jeitschko, and E. Parthe, *J. Appl. Crystallogr.* **10,** 73 (1977).
19. R. D. Shannon, *Acta Crystallogr. A* **32,** 751 (1976).
20. J. Darriet and M. A. Subramanian, *J. Mater. Chem.* **5**(4), 543 (1995).
21. J. L. Hutchison and A. J. Jacobson, *Acta Crystallogr. B* **31,** 1442 (1975).
22. J. L. Hutchison and A. J. Jacobson, *J. Solid State Chem.* **20,** 417 (1977).
23. J. L. Hutchison and A. J. Jacobson, *J. Solid State Chem.* **35,** 334 (1980).